

Spatial Break-up of Femtosecond Laser Pulses in the Atmosphere

L. Bergé^{1,*}, S. Skupin^{1,2}, F. Lederer², G. Méjean³, J. Yu³, J. Kasparian³, E. Salmon³ and J. P. Wolf³

¹Département de Physique Théorique et Appliquée, CEA/DAM Ile de France, B.P. 12, 91680 Bruyères-le-Châtel, France

²Friedrich-Schiller-Universität Jena, Max-Wien-Platz 1, 07743 Jena, Germany

³Laboratoire de Spectrométrie Ionique et Moléculaire, Université Cl. Bernard Lyon 1, UMR-CNRS 5579, F-69622 Villeurbanne cedex, Lyon, France

Received September 8, 2003

PACS Ref: 42.65.Tg, 42.68.Ay, 42.65.Jx

Abstract

The filamentation of femtosecond pulses in air is investigated experimentally and numerically for beam powers accessing several hundreds of critical powers for self-focusing. First, evolution of the filament patterns is approached by an averaged-in-time $(2D + 1)$ -dimensional model derived from the standard propagation equations for ultrashort pulses. Elementary processes such as soliton generation, dissipation by multiphoton absorption and coalescence of filamentary cells are discussed. Second, the $2D$ model is employed for reproducing filament patterns of femtosecond pulses delivered by a mobile TW laser source (TERAMOBILE). Beam propagation is shown to be driven by the interplay between intense, robust spikes aggregated around the defects of the beam and random nucleation of light cells.

1. Introduction

The long-range propagation of femtosecond (fs) laser pulses in air is a well-known phenomenon currently exploited in, e.g., remote sensing techniques [1–3]. Infrared pulses with about 100 fs duration indeed generate narrow filaments of light over long distances, which promote white-light emission allowing high-altitude absorption spectroscopy experiments [3]. This self-guiding originates from the early optical self-focusing caused by the Kerr response of air and leading to an increase of the light intensity. The beam collapse is then saturated by the electron plasma created by ionization of air molecules, when the pulse intensity reaches $\sim 10^{14}$ W/cm². For moderate input powers, P_{in} , below a few tens of critical powers for self-focusing, P_{cr} , one or two filaments are created [4–7]. At much higher powers, many filaments can be produced. This process is initiated by the modulational instability, which tends to break up the beam into small-scale cells conveying each a power close to $\pi^2 P_{\text{cr}}/4$ [8,9]. Several important mechanisms have been proposed to anticipate the dynamics of filamentary cells. On the one hand, a beam can split into a couple of spots that persist over several meters before fusing into a robust central lobe [7]. On the other hand, it has been numerically predicted [10] that collapsing light cells may be nucleated at random and defocused by plasma generation over short distances ($\ll 1$ m). Recurrent sequence of collapse events then seeds a sea of spiky filaments, which support an “optically turbulent light guide” in the medium. To the best of our knowledge, a scenario unifying both these aspects is still missing. To be valid, this scenario should be confronted with direct experimental observations.

The present work outlines major features in the filamentation dynamics of fs pulses with relatively high powers ($P_{\text{in}}/P_{\text{cr}} > 100$). To address this issue, we first derive a $(2D + 1)$ -dimensional model where solitonlike states describe short-range “randomly-nucleated” filaments. We show that these structures confine themselves into a limited number of long-range coherent objects, termed as “optical pillars”. Besides transient stages where turbulent cells recur, these new structures around which filaments self-organize drive the pulse dynamics, which is confirmed by the direct solving of the $(3D + 1)$ -dimensional equations for short-pulse propagation. Next, two series of experiments involving the Teramobile facility [2,3] are performed, engaging either moderate ($P_{\text{in}} = 120 P_{\text{cr}}$) or high powers ($P_{\text{in}} = 700 P_{\text{cr}}$). We compare each filamentation figure with results yielded by the $(2D + 1)$ -dimensional model, which faithfully restores the experimental patterns.

From the numerical point of view, we consider standard propagation equations [7,10,11]:

$$\begin{aligned} \frac{\partial \mathcal{E}}{\partial z} = & \frac{i}{2k_0} \nabla_{\perp}^2 \mathcal{E} - i \frac{k''}{2} \partial_t^2 \mathcal{E} + i \frac{k_0 n_2}{2} \\ & \times \left(|\mathcal{E}|^2 + \tau_K^{-1} \int_{-\infty}^t e^{-(t-t')/\tau_K} |\mathcal{E}(t')|^2 dt' \right) \mathcal{E} \\ & - \left(\frac{\sigma}{2} + i \frac{k_0}{2\rho_c} \right) \rho \mathcal{E} - \frac{\beta^{(K)}}{2} |\mathcal{E}|^{2K-2} \mathcal{E}, \end{aligned} \quad (1)$$

$$\partial_t \rho = \sigma_K \rho_{\text{nt}} |\mathcal{E}|^{2K} + \frac{\sigma}{U_i} \rho |\mathcal{E}|^2, \quad (2)$$

which couple an extended nonlinear Schrödinger (NLS) equation for the electric field envelope \mathcal{E} , to a Drude model for the local plasma density ρ . These equations apply to fs pulses moving in their group-velocity frame ($t \rightarrow t - z/v_g$), characterized by a beam waist w_0 , half-width duration t_p , Rayleigh length $z_0 = \pi w_0^2/\lambda_0$, and the central wavenumber $k_0 = 2\pi/\lambda_0$. The critical power for self-focusing in air takes the value $P_{\text{cr}} = \lambda_0^2/2\pi n_2 = 3.3$ GW at the laser wavelength $\lambda_0 = 800$ nm. The Kerr refraction index is $n_2 = 3.2 \times 10^{-19}$ cm²/W and the coefficient for group-velocity dispersion (GVD) reads as $k'' = 0.2$ fs²/cm. In Eq. (1), $\nabla_{\perp}^2 = \partial_x^2 + \partial_y^2$ accounts for optical diffraction in the (x, y) plane and the complete Kerr response of air is composed of an instantaneous contribution and a delayed part in ratio 1/2, with a relaxation time $\tau_K = 70$ fs [7,12]. $\rho_c \simeq 1.8 \times 10^{21}$ cm⁻³ is the critical plasma density beyond which the medium becomes opaque. Power dissipation is

*To whom correspondence should be addressed:
e-mail: luc.berge@cea.fr

assured by multiphoton absorption (MPA) with coefficient $\beta^{(K)} \simeq 4.25 \times 10^{-98} \text{ cm}^{2K-3} / W^{K-1}$ [11,12]. In Eq. (2), plasma defocusing is mainly induced by ionization of oxygen molecules with a gap potential $U_i = 12.1 \text{ eV}$ and an initial density $\rho_{\text{nt}} = 0.2 \times \rho_{\text{at}}$, contributing to 20% of the total neutral density $\rho_{\text{at}} = 2.7 \times 10^{19} \text{ cm}^{-3}$ [12]. Plasma formation is expected to be essentially driven by multiphoton ionization (MPI) with coefficient $\sigma_K = 2.88 \times 10^{-99} \text{ s}^{-1} \text{ cm}^{2K} / W^K$, where the number of photons K needed to extract electrons from neutral atoms is $K = 8$. Avalanche ionization involving the cross-section for inverse bremsstrahlung $\sigma = 5.44 \times 10^{-20} \text{ cm}^{-2}$ and related plasma absorption, although of weaker influence for fs pulses, have been included for completeness of the model.

2. Nonlinear dynamical aspects

Before proceeding, we elaborate from Eq. (1) on a reduced model constructed by averaging the temporal dependencies of \mathcal{E} . Considering subpicosecond durations, avalanche ionization and plasma absorption are here ignored. We moreover omit GVD, whose coefficient $k'' = 0.2 \text{ fs}^2/\text{cm}$ makes it too weak for being a key-player over filamentation distances limited to 100 m. Under these approximations, we assume that MPI counterbalances Kerr self-focusing at a time slice $t \simeq t_c(z)$ where a dominant spike with temporal extent T emerges among other time slices in the pulse temporal profile. This extent keeps the same order of magnitude along propagation, i.e., filaments arise as optical structures coupled with an ionization front that shrinks the pulse to the same mean duration. Because there exists evidence [13] that MPI shortens pulses to 1/10 of their initial length, we choose $T = t_p/10$, which was also recently justified in [14]. We thus set $\mathcal{E}(x, y, z, t) = \psi(x, y, z) \times \chi[t, t_c(z)]$, where the temporal distribution for the highest-intensity peak is modeled by the Gaussian $\chi[t, t_c(z)] = e^{-[t-t_c(z)]^2/T^2}$ with $T = 0.1t_p$. Plugging this expression of \mathcal{E} into Eq. (1), integrating the equation for ρ and averaging Eq. (1) over the whole time domain then provides the equation for the transverse component ψ :

$$i\partial_z \psi + \frac{1}{2k_0} \nabla_{\perp}^2 \psi + \alpha k_0 n_2 |\psi|^2 \psi - \gamma |\psi|^{2K} \psi + i\nu |\psi|^{2K-2} \psi = 0, \quad (3)$$

with $\alpha = \frac{1}{4}(\sqrt{2} + D(t_p)/\tau_K)$, $\nu = \beta^{(K)}/2\sqrt{K}$ and $\gamma = k_0 \sigma_K \rho_{\text{nt}} \sqrt{\pi/8KT}/2\rho_c$. Here, the function

$$D(t_p) \equiv \int_{-\infty}^{+\infty} e^{T^2/8\tau_K^2 - u/\tau_K - 2u^2/T^2} \times \left\{ \text{Erf} \left(\frac{\sqrt{2}u}{T} - \frac{T}{\sqrt{8}\tau_K} \right) + 1 \right\} du \quad (4)$$

follows from averaging in time the delayed Kerr contribution of Eq. (1).

Equation (3) is instructive for understanding the transverse dynamics of filamentary structures. Three key-processes must indeed be emphasized for this purpose.

- (i) In the non-dissipative case ($\nu = 0$), Eq. (3) admits soliton solutions in the form $\psi = \phi(x, y)e^{i\Lambda z}$. Characterized by an intensity reaching the saturation

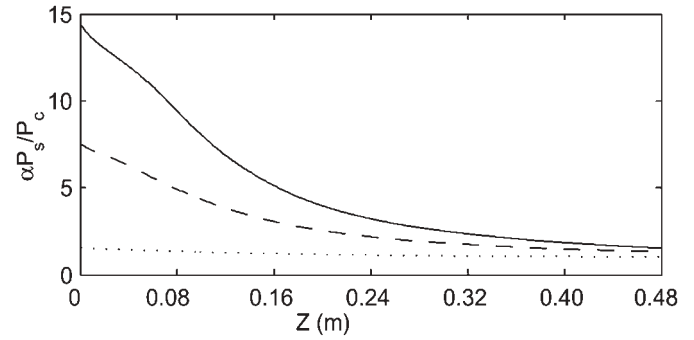


Fig. 1. Decrease of P_s versus z for the soliton states engaging $1.5 P_c/\alpha$ (dotted curve), $7 P_c/\alpha$ (dashed curve) and $15 P_c/\alpha$ (solid curve), as they undergo MPA for beam waist $w_0 = 1 \text{ mm}$.

threshold $I_{\text{max}} \sim (\gamma/\alpha k_0 n_2)^{1/1-K}$, these solitons satisfy the criterion for orbital stability $dP_s/d\Lambda > 0$ [15], where P_s is the power $P \equiv \int |\psi|^2 dr$ computed on the function ϕ . As detailed in [14], low-power solitons ($\alpha P_s/P_c < 1.5$) are close to the Townes mode of the cubic NLS equation with power $P_c \simeq 0.93 \times P_{\text{cr}}$. High-power ones ($\alpha P_s/P_c > 1.5$) exhibit a shape resembling high-order super-Gaussians (SG).

- (ii) When adding MPA ($\nu \neq 0$), the soliton power decreases continuously until reaching the effective collapse threshold P_c/α . This property is shown in Fig. 1. By modelling ϕ like $\phi = A_s e^{-(r/w_0)^{2N}}$ in monofilamentation regime ($r^2 = x^2 + y^2$, $N \geq 1$), the power relation $d_z P \simeq -2\nu \int \phi^{2K} dr$ can be solved perturbatively, in order to evaluate the dissipation range along which self-focusing persists with beam powers above critical. Computed in the limit $\alpha P_s \gg P_c$, this range:

$$\Delta z = K^{1/N} (\gamma/2\nu\alpha k_0 n_2) (1 - P_c/\alpha P_s), \quad (5)$$

is found to only vary with the laser wavelength, but not with the beam waist. It predicts a maximum filament length of 0.4 m per pulse with, e.g., $t_p = 85 \text{ fs}$ at the central wavelength $\lambda_0 = 800 \text{ nm}$, which is compatible with the short “life-time” of the recurrent filaments observed in [10] along the propagation axis.

- (iii) Solitons can mutually fuse. It can indeed be shown from the mean-square radius of the beam, $\langle r^2 \rangle \equiv \int r^2 |\psi|^2 dr / P$, that two Gaussianlike solitons with waist w_{fil} and intensity close to saturation are able to merge, even without dissipation [9]. To show this property, the two-component trial solution $\psi_{\text{in}} = \sqrt{2P_{\text{fil}}/\pi w_{\text{fil}}^2} (e^{-|r+\Delta/2|^2/w_{\text{fil}}^2} + e^{-|r-\Delta/2|^2/w_{\text{fil}}^2})$ is inserted into the “virial” expression

$$\frac{k_0}{4} P d_z^2 \langle r^2 \rangle = \frac{1}{2k_0} \int |\nabla_{\perp} \psi|^2 dr - \frac{\alpha k_0 n_2}{2} \int |\psi|^4 dr + \frac{K\gamma}{K+1} \int |\psi|^{2(K+1)} dr. \quad (6)$$

Expanding Eq. (6) by using ψ_{in} then enables us to predict that well-separated filaments ($\Delta > \sqrt{2}w_{\text{fil}}$) should fuse into a single lobe, if the total beam radius decreases in self-compression regime ($d_z^2 \langle r^2 \rangle < 0$) with dominant, exponentially-decreasing interaction terms. When the beamlet intensities attain their saturation level ($2P_{\text{fil}}/\pi w_{\text{fil}}^2 \rightarrow I_{\text{max}}$), this condition applies in particular to Gaussian-

shaped solitons satisfying

$$\alpha \frac{P_{\text{fil}}}{P_c} \leq \frac{[1 + (1 - X)e^{-X}]/0.93}{1 + 3e^{-2X} + 4e^{-3X/2} - \frac{2K}{(K+1)^2}(1 + 2(K+1)e^{-(2K+1)X/(K+1)})}, \quad (7)$$

where $X \equiv \Delta^2/2w_{\text{fil}}^2$. Plotting Eq. (7) would show that coalescence occurs between filaments mutually separated by the distance $\Delta \leq \Delta_{\text{lim}} = \sqrt{10}w_{\text{fil}}$, provided their individual powers are below a threshold evaluated nearby $1.35 \times P_c/\alpha$. For wide separation distances ($\Delta \gg \Delta_{\text{lim}}$), exponential terms in Eq. (6) vanish and the solitons should in principle cease to interact.

To illustrate this property, Figs. 2(a)–(d) show iso-intensity plots of two identical solitons with $P_{\text{fil}} = 1.3 P_c/\alpha$, $w_{\text{fil}} = 0.12$ mm (Fig. 2(a)) and $P_{\text{fil}} = 4 P_c/\alpha$, $w_{\text{fil}} = 0.2$ mm (Fig. 2(b)–(d)). The total beam waist enclosing both filaments is $w_0 = 1$ mm ($z_0 \simeq 4$ m). Two separation distances are selected, namely, $\Delta = 0.8$ mm and $\Delta = 0.6$ mm. For the first separation, lower-power solitons with no MPA were observed to evolve without interaction like stable, uncorrelated waveguides over at least 8 m (not shown here). In contrast, for the second distance approaching the critical value $\Delta_{\text{lim}} \sim 0.4$ mm, the same

solitons start to fuse at large distances $z \sim z_0$ (Fig. 2(a)). With $\Delta = 0.6$ mm, higher-power solitons do not form a steady-state waveguide by coalescence ($\Delta \sim \Delta_{\text{lim}}$). Instead, they combine into a breatherlike structure having a stable internal oscillating mode (Fig. 2(b)). This mode generically takes place at high power levels and disappears to the benefit of a stationary waveguide as soon as $P_{\text{fil}} < 2P_c/\alpha$. When $\Delta = 0.8$ mm exceeds $\Delta_{\text{lim}} \simeq 0.6$ mm, solitons with four critical powers propagate without correlation (Fig. 2(c)). In the presence of MPA (Fig. 2(d)), however, the power in each of those solitons rapidly decreases below $2P_c/\alpha$, which finally promotes their mutual coalescence. These behaviors are in reasonably-good agreement with the previous theoretical expectations. Nonetheless, discrepancies arised, which are linked to the modeling of soliton shapes by Gaussian functions with saturated intensities. More precisely, the self-compression requirement $d_z^2 \langle r^2 \rangle < 0$, computed with real soliton profiles instead of Gaussians, was found to hold over a large interval of powers, even for separation distances satisfying the criterion $\Delta \leq \Delta_{\text{lim}}$. The upper bound of power for coalescence suggested by Eq. (7) could not be verified numerically and direct simulations showed that solitons with powers clearly above $1.35 P_c/\alpha$ were indeed able to merge when $\nu = 0$.

The last configuration shown in Fig. 2(d) deserves a special comment: As can be seen from this figure, the propagation length of the solitons before their merging

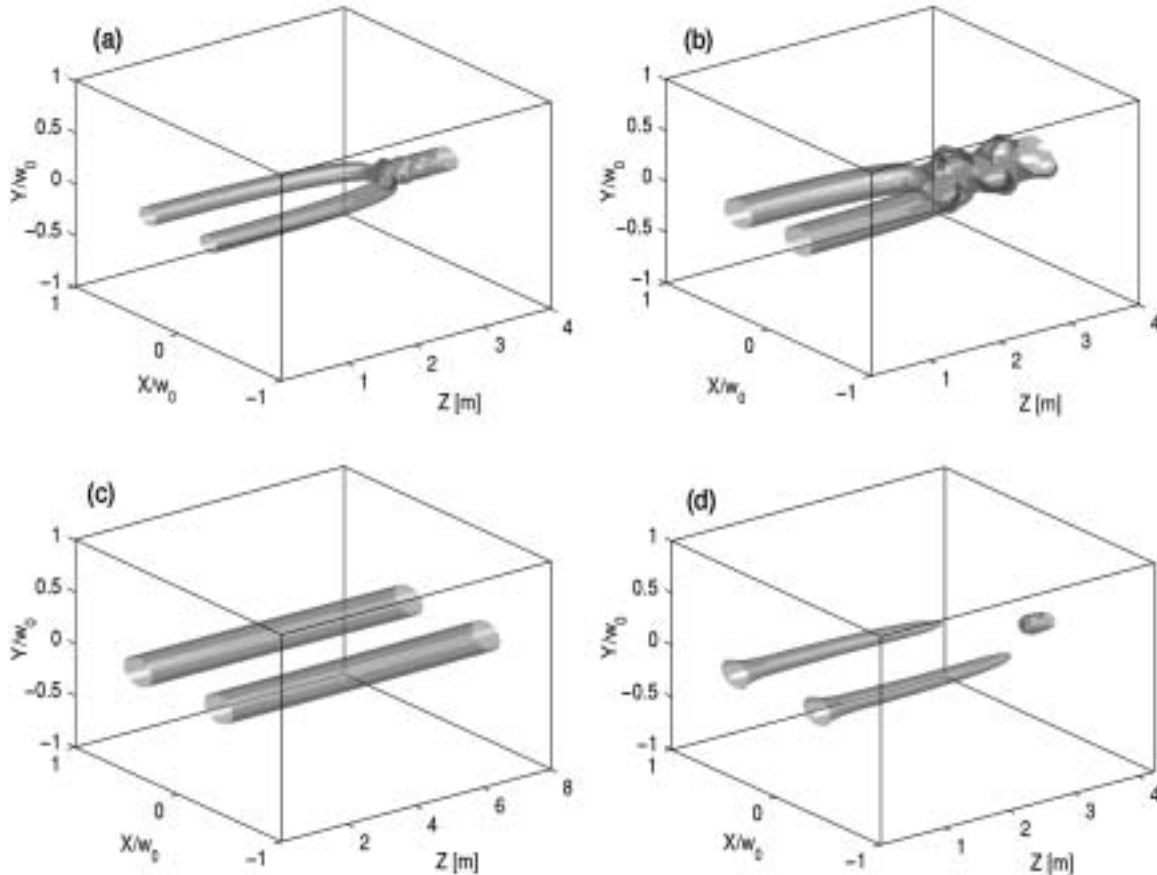


Fig. 2. Interaction of two solitons for different powers and separation distances. (a) Fusion of conservative solitons with individual power $P_{\text{fil}} = 1.3 P_c/\alpha$ ($w_{\text{fil}} = 0.12$ mm) and $\Delta = 0.6$ mm. Filaments were observed to propagate without fusing for $\Delta = 0.8$ mm. (b) Oscillations of merging solitons when their power is increased to $4 P_c/\alpha$ for the small separation $\Delta = 0.6$ mm and no MPA. (c) Uncorrelated propagation of two conservative solitons with $4 P_c/\alpha$ when their separation distance is increased to $\Delta = 0.8$ mm. (d) Fusion of solitons subject to MPA with $P_{\text{fil}} = 4 P_c/\alpha$ and $\Delta = 0.8$ mm.

widely exceeds (by almost one decade) the damping length (5) computed for one isolated waveguide (Fig. 1). Visual inspection of the soliton shapes allows us to justify this surprising behavior. As power goes down to critical through MPA dissipation, the solitons glide down along the curve (P_s, Λ) by modifying their spatial shape, whose tail becomes more and more extended in space. They can thereby overlap and produce a third lobe at center, which will raise all the farther along z as the initial separation Δ is large. This particular dynamics can help groups of neighboring filaments to survive over several meters in filamentation patterns.

The above properties dictate the filament dynamics. As an example, Fig. 3 illustrates filamentation patterns in the 2D approximation, for which the input beam shape undergoes random, isotropic perturbations. By comparison with antecedent experimental data [7,16], we opted for an input anisotropic N th-order SG beam in the form $\psi = \sqrt{I_0} e^{-(x^2/w_0^2 + 2y^2/w_0^2)^N}$, perturbed at $z = 0$ by an isotropic 10% random noise in amplitude, multiplied by a 10% noisy Gaussian temporal profile with $t_p = 85$ fs. The fluence distribution $[F = \int_{-\infty}^{+\infty} |\mathcal{E}(t)|^2 dt]$ of the resulting beam is then employed as the input datum for Eq. (3). Figure 3(a) shows the iso-intensity plots for a perturbed beam with waist $w_0 = 2$ mm, $N = 2$ and $P_{in} = 95 P_c$. The beam first gives rise to several short-scale collapsing filaments. Intermittency in filament nucleation occurs in the early propagation stage over short ranges ≤ 0.5 m, which can be compared with the scenario of optical

turbulence proposed in [10]. Nevertheless, at larger distances, the filaments gather into a limited number of channels. The output filaments reach the maximum intensity I_{max} over distances $\sim \Delta z$, but they asymptotically remain captured in longer soliton envelopes that form “optical pillars” in the medium. By “optical pillars”, we mean discrete light spots capable of amalgamating solitonlike cells that self-attract around specific points in the diffraction plane. The resulting structure then sustains a long-range propagation, while it can still continue to excite short-living cells in its neighborhood. In the present configuration, the filamentary structures organize the entire beam into three major long-range pillars composed of solitonlike filaments.

By comparison, Eqs. (1) and (2) are now resolved in $(3D + 1)$ -dimensional geometry by means of a spectral code using fast Fourier transforms in the (x, y, t) variables. Integration along the longitudinal axis (z) is performed with an adaptive step tuned on the intensity growth. 2048 points in the time direction and 1024 points along both transverse axes were required for a numerical box with length of $8w_0$. Figure 3(b) represents the plasma strings produced by the previous beam. The temporal pulse profile, even subject to strong distortions, does not prevent the transverse dynamics of the pulse from developing as in Fig. 3(a), up to second-order discrepancies in the focus point linked to the choice of T . Although different temporal slices come into play, all of them support the propagation of cells first nucleated at different locations, then remaining localized around the *same* place in the (x, y) plane. Three distinct channels clearly emerge: They do not interact significantly but remain almost robust at their transverse position.

In view of the above results, the multiple filamentation of fs pulses can be sketched as follows: (i) Beam modulations give rise to short-range filaments that grow in intensity until reaching the ionization threshold I_{max} . In this limit, near-soliton filaments, searching for an equilibrium position, recur in an optically-turbulent regime during the early stage of propagation [10]. (ii) As they attain a quasi-stable configuration with respect to their neighbors, short-range filaments either fuse or self-attract without merging, depending on their inner power and mutual separation distance, in order to form a limited number of clusters named “optical pillars”. These propagate over longer distances. It is important to note that the present scenario applies to input beams where *an isotropic random noise* first creates short-scale cells, which afterwards relax to quasi-coherent structures. For experimental beams exhibiting salient defects at $z = 0$, the location of optical pillars in the transverse plane may be preconditioned by the most intense defects, which can further excite turbulent cells in their vicinity, as seen below.

3. Numerical simulations versus experiments

From the experimental point of view, we investigate evolution stages in the filamentation pattern produced by the TERAMOBILE laser [2]. This system delivers at the 10 Hz rate pulses with energy up to 0.5 J, transverse diameter equal to 5 cm ($w_0 \simeq 2.5$ cm), and FWHM durations ($= \sqrt{2 \ln 2} t_p$) tunable from 100 fs to 600 fs by

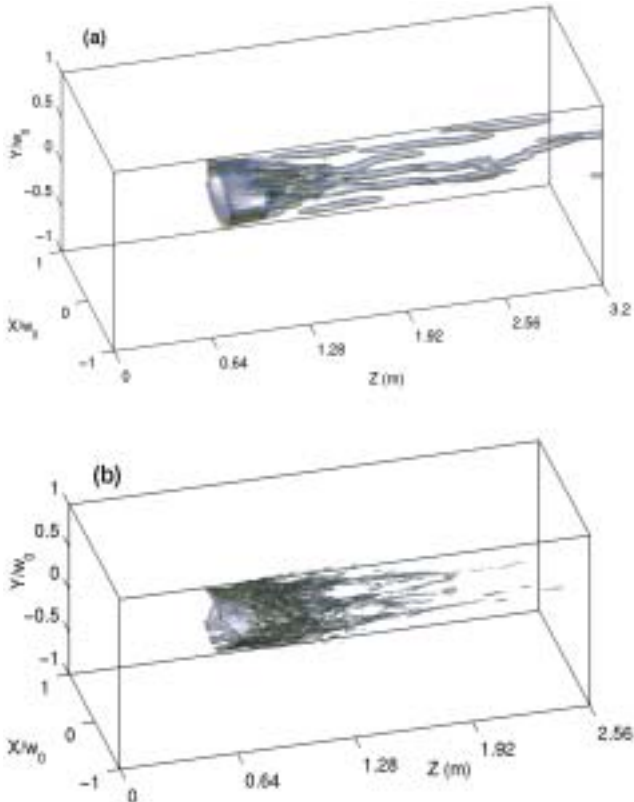


Fig. 3. (a) Iso-intensity patterns of filamentary structures created from an SG beam governed by the 2D reduced model with $N = 2$, $P_{in} = 95 P_c$ and $w_0 = 2$ mm. (b) Plasma strings produced by the same beam integrated from the $(3D + 1)$ -dimensional Eqs. (1) and (2).

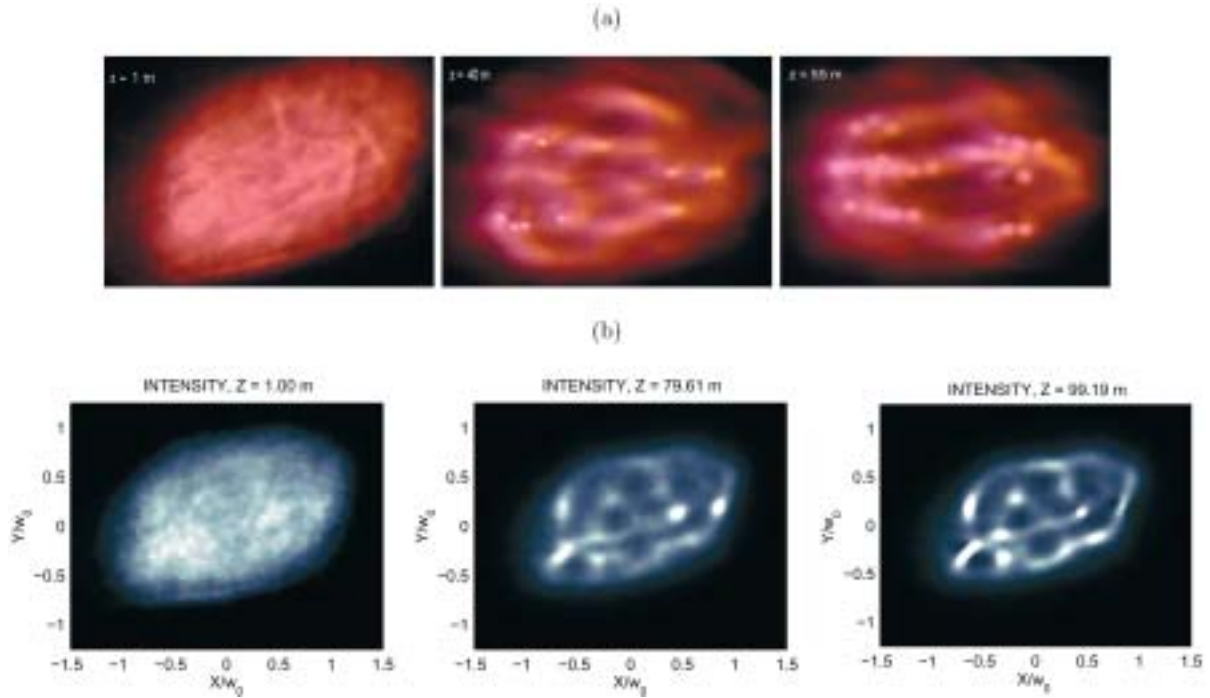


Fig. 4. Filamentation patterns (a) produced experimentally for the $120 P_{\text{cr}}$ beam at $z = 1, 40$ and 55 m. (b) Numerical computations of the same beam from Eq. (3). Maximum intensity is limited to twice the input intensity, in order to clearly underline the positions of the optical pillars arising from the beam defects.

detuning the compressor with a chirp opposite to air dispersion. Experiments show photos taken in open air from a white screen positioned in the plane orthogonal to the beam path. A filter with narrow bandwidth around the fundamental wavelength $\lambda_0 = 800$ nm was put in front of the camera. Two photos with exposure time of $1/8$ th second were taken in sequence at each longitudinal distance, so that two pulses could alter the pattern in some pictures. No qualitative change, however, was observed, up to slightly more visible filaments at certain distances.

Figure 4(a) details the growth of light filaments over 55 m with 230 mJ energy and pulse duration of 600 fs ($P_{\text{in}} \approx 120 P_{\text{cr}}$). At the edge of the beam where fluctuations are the most intense, filaments emerge from local defects and several cells occur along a flattened ring inside the focal spot [$z = 40$ m]. More filaments are then generated around this ring: They aggregate around the spots created at $z = 40$ m and finally evolve into a three-pronged fork shape at $z = 55$ m.

Figure 4(b) illustrates numerical simulations obtained by solving the $(2D + 1)$ -dimensional Eq. (3) from a data file of the experimental input beam. With a pulse duration of 600 fs ($t_p \approx 510$ fs), the coefficient α in Eq. (3), computed from Eq. (4), takes the value $\alpha = 0.51$. The beam begins to form local clots from the highest intensity regions in a fashion similar to Fig. 4(a). The final pattern, involving several small-scale spots, results in a trident-shaped figure, restoring thereby the experimental observation. The discrepancy existing between the experimental distances and their numerical counterparts is attributed to our former choice $T = 0.1 t_p$. This choice suits the experimental development of filaments in ionization regime, but cannot restore the early self-focusing distances of beams with moderate powers,

requiring rather $T = t_p$. For such beams engaging 120 critical powers only, Eq. (3) describes the filamentation of a disordered optical distribution with an effective ratio of input power over critical of about $\sim \alpha P_{\text{in}}/P_{\text{cr}} \approx 60$. This limits to about 24 the number of genuine filaments reaching the ionization threshold. From the numerical as well as experimental images, we can observe that the most intense filamentary channels, forming “optical pillars” in the medium, persist over several tens of meters, whereas secondary light cells are randomly nucleated over shorter longitudinal scales.

Reducing the pulse duration to 100 fs ($t_p = 85$ fs) makes it possible to investigate filamentary patterns promoted by fs beams with powers as high as $700 P_{\text{cr}}$. In this case displayed in Fig. 5(a), the beam breaks up into more cells than in the previous lower-power case. Following the estimate recalled in the introduction, up to $\alpha P_{\text{in}}/P_{\text{fil}} \sim 110$ light cells may form in principle with $P_{\text{fil}} \approx \pi^2 P_{\text{cr}}/4$. Figure 5(b) reproduces these experimental patterns from a numerical integration of Eq. (3) performed with the parameter $\alpha = 0.39$ fixed by $t_p = 85$ fs. The agreement between the experimental and numerical results is quite satisfactory. These patterns reveal that, although some filaments are able to survive over several meters at the most powerful regions of the pulse [$z = 30$ m and 35 m], random nucleation of filaments in the entire focal spot seems more privileged, compared with the break-up of the former $120 P_{\text{cr}}$ beam. We explain this property by the partial inhibition of the fusion mechanism between filamentary cells (see Section 2), which convey each a higher power and experience more substantial power transfers through the overall surface of the beam. Finally, we can remark that robust filaments surviving over longitudinal distances ≥ 5 m evolve in correlation with close, but spatially-separable

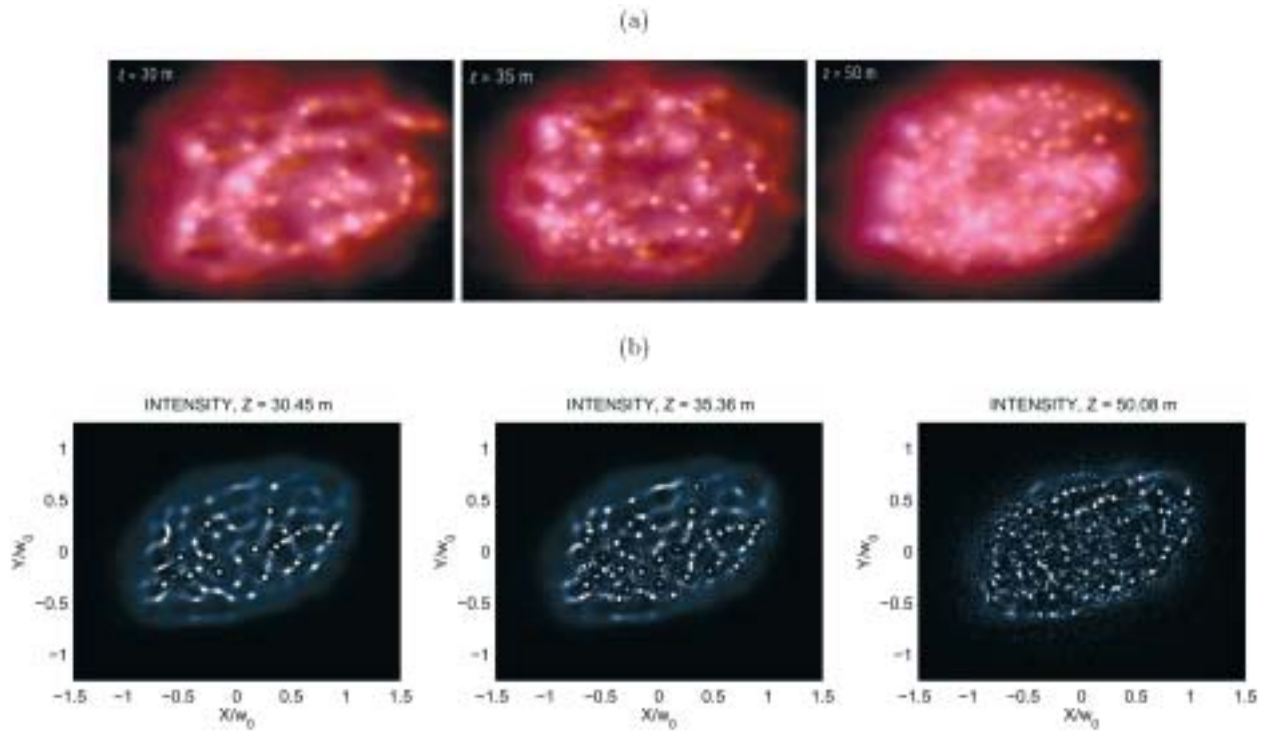


Fig. 5. Filamentation patterns (a) produced experimentally for the $700 P_{cr}$ beam at $z = 30, 35$ and 50 m. (b) Numerical computations of the same beam from Eq. (3).

neighbors, from which they can develop a long-range propagation dynamics resembling that displayed by Fig. 2(d).

4. Conclusion

In summary, we have investigated the multiple filamentation of high-power beams, both theoretically and numerically. In the experiments, pulses were delivered by the TERAMOBILE laser able to access TW powers. Recent experiments on the beam break-up were already performed by means of the same facility for pulse powers as high as $1000 P_{cr}$ and compared with numerical simulations [14]. In the present scope, we analyzed intermediate power levels limited to $700 P_{cr}$ and concentrated more thoroughly on the various interaction regimes that filaments may undergo. Generic features are refound throughout both these works. Long-range filaments are initiated either asymptotically after an early stage of random nucleation for isotropically-perturbed beams or by the most intense defects of experimental beams. The resulting channels, termed as “optical pillars”, can persist over several tens of meters. Around these channels, small-scale spots arise and recur rapidly at other places in the diffraction plane, in agreement with the scenario of “optically-turbulent light guides” proposed in [10]. Long-living filaments, as well as unstable randomly-nucleated ones, can be described by the reduced 2D model [Eq. (3)], which reproduces the experimental patterns. To conclude, let us emphasize that, throughout this investigation, the beams were emitted in parallel geometry. It is thus not excluded that a reduction of the beam waist through an appropriate

convergent lens may allow to generate longer light channels, by gathering all filamentary components into a single central spot. This point, requiring a parametric study depending on the beam aperture, will be addressed in a forthcoming work.

Acknowledgements

The authors thank Cl. Gouédard for preparing data files of the experimental input beams. Experiments were performed in the framework of the TERAMOBILE project, funded jointly by CNRS and DFG.

References

1. Wöste, L. *et al.*, Laser Optoelektronik **29**, 51 (1997).
2. Wille, H. *et al.*, Eur. Phys. J. Appl. Phys. **20**, 183 (2002).
3. Kasparian, J. *et al.*, Science **301**, 61 (2003).
4. Braun, A. *et al.*, Opt. Lett. **20**, 73 (1995).
5. LaFontaine, B. *et al.*, Phys. Plasmas **6**, 1615 (1999).
6. Chin, S. L. *et al.*, Appl. Phys. B **74**, 67 (2002).
7. Tzortzakis, S. *et al.*, Phys. Rev. Lett. **86**, 5470 (2001).
8. Bespalov, V. I. and Talanov, V. I., J. Exp. Theor. Phys. Lett. **3**, 307 (1966).
9. Bergé, L., Gouédard, Cl., Schjødt-Eriksen, J. and Ward, H., Physica D **176**, 181 (2003).
10. Mlejnek, M., Kolesik, M., Moloney, J. V. and Wright, E. M., Phys. Rev. Lett. **83**, 2938 (1999).
11. Mlejnek, M., Wright, E.M. and Moloney, J. V., Opt. Lett. **23**, 382 (1998).
12. Couairon, A. *et al.*, J. Opt. Soc. Am. B **19**, 1117 (2002).
13. Ward, H. and Bergé, L., Phys. Rev. Lett. **90**, 053901 (2003).
14. Skupin, S. *et al.*, submitted to Phys. Rev. E (2003).
15. See for review: Bergé, L., Phys. Rep. **303**, 259 (1998).
16. Mondelain, D., PhD Thesis No. 212-2001, Université Cl. Bernard—Lyon 1—France, p. 121 (2001).